Rapid sea level rise along the Antarctic margins driven by increased glacial discharge

Supplementary material

Uncertainty in SSH measurements and trends

The measurement of SSH from satellite altimeters suffers from multiple sources of uncertainty. These are reviewed extensively elsewhere[30] and are therefore only summarised here. One of the largest sources of uncertainty in the altimetric data sets of sea level anomaly is that arising from the frame of reference used to correct for the satellite's orbit error[30-32]. Preceding estimates of this orbit error for the TOPEX / Jason satellites are as high as 1.5 mm yr^{-1} in the z-direction (31), although this error is thought to be smaller for more recent data processing. Here we assume an upper limit of 1 mm yr^{-1}. The orbit correction is known to be symmetric along the z-axis. For a z-translation the error is proportional to the sine of the latitude; therefore, an error of magnitude 1 mm yr^{-1} gives a value of 0.9 mm yr^{-1} at 65 °S, and a difference of 0.09 mm yr^{-1} between 65°S and 75°S. From this small difference, it is clearly not possible to produce the narrow band of increased sea level observed (Fig. 1). The lower orbit heights of ERS and Envisat result in larger orbit errors, particularly in the y-direction, but the dominant role of TOPEX / Jason observations in the AVISO gridded data essentially eliminates this error, which has also greatly reduced in recent solutions. Additionally, the altimetric data north of 62°S have been re-processed with an improved frame of reference that reduces orbit errors[33]. The sea level anomaly data in the Antarctic subpolar seas north of 62°S are well correlated ($p > 99\%$) with this improved data set, and our sea level rise estimates in that region are unchanged.

Following orbit error, the main sources of uncertainty in SSH trend are the wet troposphere correction, and the biases applied to link together SSH records from different altimeters[30]. The wet troposphere error is a function of atmospheric water content and therefore latitude; it can be as high as 2 mm yr^{-1} in the tropics but is negligible at high latitudes[30]. Further, the biases applied to link together SSH records from different altimeters[30] contribute an uncertainty for the reference TOPEX / Jason missions of about 0.15 mm yr^{-1}. Other sources of uncertainty, such as instrumental, meteorological, and tide-related factors contribute less than 0.1 mm yr^{-1} (ref. 30).

Since the geographical variability of some potentially significant sources of uncertainty (particularly those associated with the satellite orbit calculation and the bias between different satellite missions) has not been accurately characterized for the AVISO data set (see e.g., discussion in ref. 30-34), here we adopt a multi-line approach to further demonstrate the robustness of the signal of anomalously rapid sea level rise in the Antarctic subpolar seas at the core of this study.

First, the relative significance (assuming negligible systematic error) of the linear trend in SSH for each data point in the gridded AVISO data set is estimated with a Patterson t-test accounting for auto-covariance in the sea level record (Fig. S1). This indicates that, in general, the Antarctic coastal sea level rise signal is significantly different from zero with 95% confidence, with some exceptions in areas of weak anomalous sea level rise in the Amundsen Sea, eastern Ross Sea and Weddell gyre.

Second, we show that the Antarctic coastal sea level rise signal is present in the measurements of individual satellite missions (Fig. S2). To do this, we consider the along-track SSH data recorded by the ERS-1, ERS-2 and Envisat altimeters, as obtained from the Centre National d'Etudes Spatiales (CNES)[18]. These data sets have had the aforementioned corrections applied, but have not been cross-calibrated in the same way as the merged data set. We select regions of significant anomalous sea level rise (identified on the basis of Fig. S1) and bin-average single-track measurements for every intersection of the satellite track with each specified area, typically every 10 days. The resulting SSH time series are illustrated by Fig. S2, which shows the single-mission sea level records in the western Ross Sea, representative of that in other regions inspected. The presence of an anomalous sea level rise signal that is both consistent between different satellites and highly coherent with the gridded AVISO data set indicates that the Antarctic coastal sea level rise signal does not arise from uncertainty in the bias between different missions.

Finally, we emphasize that the Antarctic coastal sea level rise signal identified in this study has a spatial footprint that is both distinct from those of any known sources of uncertainty in altimetric measurements and consistent with expectations from numerical simulations of the present deglaciation of Antarctica[35-36]. This provides further endorsement for the inference that the signal is of physical origin. Following these arguments, the combination of dominant error terms suggests an overall regional average error of 1-1.5 mm yr^{-1}, and an error of 0.2-0.6 mm yr^{-1} for the difference between 65°S and 75°S. In the main text we use the upper bounds of these values.

Impact of glacial isostatic adjustment

Despite correcting for a number of measurement errors, the sea level anomaly products do not intrinsically correct for changes in the geoid, of which the dominant component is glacial isostatic adjustment (GIA). This correction is estimated using output from a GIA model[37] (Fig. S3) and subtracted from the MSLA fields before analysis. In addition, an estimate of the more recent changes in the geoid resulting from e.g., mass loss from the Antarctic Peninsula, is made. The recent geoid trend is estimated by subtracting the GIA correction from the total GRACE geoid correction[38] (Fig. S3). This provides an estimate of recent changes to the geoid over the GRACE period (2003-2011). As the altimetric record is initiated in 1992, the recent geoid correction cannot be easily compared and thus directly subtracted from the altimetric data. The recent geoid correction shows a strong negative anomaly with a maximum of ~ -2 mm yr^{-1} in the Amundsen - Bellingshausen region, and a weaker positive anomaly of ~ 0.5 mm yr^{-1} between the Weddell Sea and the Amery region. An Antarctic subpolar sea-mean of this correction yields -0.2 mm yr^{-1}, which is subtracted from the circumpolar-average subpolar sea level anomaly and accounted for in its error budget. A direct subtraction of this correction would increase the SSH trend anomaly in the Amundsen - Bellingshausen region, and decrease it in East Antarctica, thereby enhancing the agreement between observational and model results.

Impact of temporal aliasing of SSH measurements

Our calculation of the linear trend in summertime SSH over the 1992-2011 period incorporates all data points between January and April not covered by sea ice. Summertime sea ice cover across the Antarctic subpolar seas is, however, highly variable in both space (i.e. the regularity of sea ice cover varies with location across the Antarctic subpolar seas) and time (i.e. at any given location, there may be substantial intraseasonal and interannual variability in sea ice cover), so that any estimate of interdecadal SSH change in the region may be affected by aliasing. Indeed, there are significant regional trends in Antarctic summertime sea ice extent during this period[3].

In order to show that our results are robust to this aliasing issue, the time series of circumpolar-mean SSH anomaly south of the oceanic boundary of the Antarctic coastal sea level rise signal (Fig. 2) is compared with a time series of SSH anomaly averaged over the ~5% of that region that is ice-free over the entire altimetric record (Fig. S4). The two time series are in good agreement, and exhibit a high correlation coefficient of 0.8. Further, the ice-free time series confirms the existence of a strong seasonal cycle in Antarctic coastal sea level, discussed in the main text.

Global-mean sea level rise

In this work, the rate of sea level rise in the Antarctic subpolar seas is calculated by subtracting the rate of global-mean *total* sea level rise, ~3.2 mm yr^{-1}, from the linear trend in SSH. The rate of global-mean *total* sea level rise is computed as an area-weighted average of the AVISO-gridded sea level anomaly data over austral summer months only. Global-mean sea level rise results from the combined effect of barystatic and steric contributions. Barystatic changes in sea level are rapidly communicated away from their source and so are considered global[36]. Steric changes are less effectively communicated and remain more regionally confined over the two-decade time scale relevant to our study. It is unlikely that the global-mean rate of barystatic sea level rise accounts for more then half of the trend in total sea level (ref. 20-21), requiring a steric contribution of ~1.5 mm yr^{-1} to balance the budget. While in the tropics the majority of this steric signal is readily accounted for by upper-ocean warming, the thermal expansion coefficient for seawater decreases in polar regions and salinity dominates steric sea level changes there. Thus, in seeking to quantify polar steric anomalies, subtracting the global-mean rate of barystatic (rather than total) sea level rise is more appropriate (Fig. S5). However, since the global-mean rate of barystatic sea level rise suffers from substantial uncertainty, in this study we discuss only the more conservative estimate relative to the global-mean rate of sea level rise.

Estimation of halosteric SSH change from *in situ* observations

Our assessment of the halosteric contribution to the observed sea level rise signal involves the estimation of steric SSH change from several *in situ* observations of interdecadal ocean freshening available within the region of the signal (Fig. 1). The estimation of halosteric change in sea level, h_s, relies on the use of a linear approximation to the equation of state[39],

$$h_s = -\beta \, \Delta S \, h_0 \qquad (1)$$

where $\beta = 7.6 \times 10^{-4}$ is the haline contraction coefficient, ΔS is the change in salinity observed in situ, and h_0 (m) is the depth over which the change in salinity has occurred.

Ocean circulation model experiments

The NEMO (Nucleus for European Modelling of the Ocean; ref. 40) model was used to assess our physical interpretation of the observed Antarctic coastal sea level rise signal. Our model configuration has a 1° resolution tri-polar grid (ORCA1). NEMO is a z-level Boussinesq ocean model (OPA) coupled to a dynamic-thermodynamic sea ice model (LIM2), and uses a linear free surface. Precipitation and evaporation affect the model via volume input through the ocean surface, and therefore influence sea surface height both through volume input and steric forcing. The model has 75 vertical levels, is forced by CLIVAR/WGOMD Coordinated Ocean-sea ice Reference Experiments (COREII) atmospheric reanalysis data, and utilises the Gent-McWilliams eddy parameterisation[41].

The model was qualitatively validated by comparison to a Southern Ocean climatology based on *in situ* measurements, the CSIRO Atlas of Regional Seas (CARS; ref 42; Figs. S6-S9). Here we compare the NEMO annual-mean fields for 1992 with the CARS mean fields, which are derived from the last 50 years of measurements. The data and model agree surprisingly well, most notably in the zonal-mean diagnostics (Fig. S8-S9). Fig. S7 contrasts the bottom distributions of temperature and salinity in the model with those in the CARS climatology, and illustrates the model's satisfactory degree of realism, particularly as regards the salinity and density fields, though bottom temperatures are too cold in the Pacific sector. Further information on and extensive validation of the model are provided in ref. 43.

Here we consider two types of model runs: a standard control run, and several perturbation runs. The control run is the last 15 years (1992–2007) of the last of four cycles of the CORE2 forcing dataset from 1948-2007, so has been spun up for 225 years[43]. A time-invariant runoff from Antarctica of 0.073 Sv, or 2200 Gt yr^{-1} (ref. 41), is assumed. The perturbation runs are identical to the control run, except for an additional surface freshwater flux anomaly applied on a 8° by 2° area centred on the Amundsen – Bellingshausen continental shelves. A total of three perturbation experiments are conducted, with surface freshwater flux anomalies of ~300 (the measured approximate excess Antarctic freshwater discharge averaged over the last 20 years, see main text), 550 and 900 Gt yr^{-1}. The SSH and steric anomalies resulting from the anomalous freshwater forcing in these runs were evaluated by subtracting the relevant physical fields in the control run from those in the perturbation runs. The linear trends in SSH, and the halosteric and thermosteric components of sea level change, were then calculated from the pertinent anomaly fields.

The key results for the 300 Gt yr^{-1} perturbation run are illustrated in Figures 3 and S6. The simulated linear trend in SSH anomaly agrees well with observations, both in magnitude and in spatial distribution. This distribution is also consistent with those in the perturbation experiments with more vigorous freshwater forcings, with the magnitude of the SSH response scaling approximately linearly with the amplitude of the freshwater forcing anomaly, echoing the findings of ref. 35-36. In all runs, the halosteric and thermosteric contributions each account for approximately 50% of the local SSH trend anomaly (i.e. the barystatic response is spatially uniform and therefore does not contribute significantly to the local anomaly in the Antarctic subpolar seas). A vertical decomposition of the steric constituents reveals that the halosteric change occurs primarily in the upper ocean (approximately half of the vertically integrated halosteric change is accounted for by the uppermost 300 m), whereas the bulk of the themosteric signal occurs in the deep ocean. This result is broadly consistent with the analyses of *in situ* observations described in the main text.

While the general endorsement of our physical interpretation of the observed Antarctic coastal sea level rise signal by the model experiments is reassuring, two significant caveats must be noted. First, there are resolution-related limitations to the model's representation of the narrow boundary current surrounding Antarctica, which is thought to play a significant role in mediating the transmission to the deep ocean of freshwater anomalies on the Antarctic continental shelves. Second, the simulated deep-ocean thermosteric changes are likely to result from variations in the formation and circulation of Antarctic Bottom Water, the production of which NEMO (like most ocean circulation models) fails to represent in a realistic fashion.

The Munk multiplier

Here we use first-principle arguments, assuming a linear equation of state approximation, to estimate the amount of freshwater required for a given steric SSH signal. This topic is discussed in depth by ref. 24.

The definition of steric height anomaly in pressure coordinates is the integral between atmospheric pressure (ap) and bottom pressure (bp), of the specific volume anomaly, v_f-v_ρ:

$$\Delta h_s = \int_{ap}^{bp} \frac{v_f - v_\rho}{g}\, dp\ , \qquad (2)$$

where $v_s = \frac{1}{\rho}$ is the specific volume of seawater, v_f is the specific volume of fresh water, and g is gravity.

The mass anomaly associated with a freshwater release in the Antarctic subpolar seas is assumed to be locally negligible as it is rapidly communicated to the global ocean, establishing a global barystatic equilibrium within ~14 days[36]. Thus, as there is negligible change in bottom pressure following a freshwater release, equation (2) then simplifies to an integral over the freshwater layer (from ap, to the base of the freshwater layer, lp).

Further, we note that

$$\int_{ap}^{lp} dp = lp - ap = \rho_f\, g\, \delta h\ , \qquad (3)$$

and as $\frac{v_f - v_s}{g}$ is constant (2) becomes

$$\Delta h_s = \rho_f\, g\, \delta h\, \frac{v_f - v_s}{g}\,. \quad (4)$$

After some re-arrangement, we find

$$\Delta h_s = \frac{\delta h(\rho_s - \rho_f)}{\rho_s}\,, \quad (5)$$

and

$$\Delta h_s = (1 - \frac{\rho_f}{\rho_s})\delta h\,. \quad (6)$$

Following equation (6), the change in steric height of the water column is then

$$\Delta h_s \approx \delta h \beta s_s. \quad (7)$$

Therefore, the amount of freshwater required to produce a given change in steric height in the Antarctic subpolar seas is

$$\delta h \approx \Delta h_s \frac{1}{\beta} s_s = \Delta h_s \cdot 37.6\,. \quad (8)$$

This equation states that for a given freshwater discharge, the resultant steric change in SSH is 37.6 times smaller than the height of freshwater added.

Tertiary mechanisms of sea level rise

In addition to the mechanisms contributing significantly to Antarctic coastal sea level rise (halosteric adjustment to an acceleration in freshwater discharge from Antarctica, and thermosteric response to the warming of the deep Southern Ocean), discussed in the main text, we have assessed the likely importance of other candidate mechanisms contributing to our observed signal.

Thermosteric adjustment to upper-ocean warming

A possible forcing of anomalous sea level rise in the Antarctic subpolar seas is a regional increase in the mean temperature of the ocean. Satellite measurements of sea surface temperature do not suggest coherent circumpolar warming of the upper-ocean waters of the subpolar seas over the last two decades[44]. In addition, *in situ* temperature measurements in the Ross Sea, a region of anomalously rapid sea level rise (Fig. 1a), show a negligible thermosteric sea level rise between 1958 and 2008 for upper-ocean waters (200-800 m; ref. 45). It is therefore likely that surface warming does not contribute significantly to the sea level trends examined here.

Halosteric adjustment to changes in precipitation and sea ice volume

There is currently no evidence to suggest significant contributions to halosteric sea level rise in the Antarctic subpolar seas from non-glacial sources. A widespread increase in Antarctic precipitation is a common result of climate models simulating the atmospheric response to changes in global climatic forcing over the late 20th and the

21st centuries[46-47], yet atmospheric reanalyses have thus far proven too uncertain to detect whether this predicted precipitation increase is presently underway[46]. Similarly, the possibility that a significant reduction in sea ice volume may have contributed to halosteric sea level rise cannot be definitively excluded due to the scarcity of sea ice thickness measurements, but it seems highly unlikely given satellite observations that show Antarctic sea ice area increasing slightly over our study period[3]. In fact, a modelling study that assimilated these sea ice concentration data indicated an increase in sea ice volume[48].

Barystatic response to variable wind forcing

Another possible cause of the observed sea level rise anomaly is a barystatic adjustment to perturbed wind forcing. Prevalent westerly winds along the northern boundary of the Antarctic subpolar seas drive a northward Ekman transport that exports water from the region, establishing a mean sea level slope upwards to the north[49]. Any reduction in the intensity of the northward Ekman transport would thus cause a relative increase in sea level close to Antarctica by allowing this slope to relax.

The SSH impact of variability in wind forcing was investigated using ERA-Interim reanalysis data[50], following comparison to other reanalysis products[51], as well as verification of this product's winds and their trends against sea-ice drift measurements[52] and *in situ* observations[53]. A time series of monthly values of the mean SSH anomaly in the Antarctic subpolar seas shows a significant correlation with a record of cross-boundary northward Ekman transport (Figs. S10-S11; $r^2 = 0.5$), with a linear gradient of $-(3.8 \pm 0.6) \times 10^{-4}$ mm (Gt yr^{-1})$^{-1}$. The linear trend in annual-mean northward Ekman transport out of the region is -480 ± 140 Gt yr^{-2} (i.e. a decrease in export) between 1992 and 2011, implying that a barystatic adjustment to wind forcing contributed 0.2 ± 0.1 mm yr^{-1} of sea level rise in the Antarctic subpolar seas relative to the rest of the ocean, a minor fraction (20% at most) of the observed signal. Repeating this analysis at a circumpolar contour following the 3000-m isobath (Fig. 1a) yielded very similar results.

The frequency dependence of the relationship between Antarctic coastal sea level and Ekman transport can be assessed by temporally averaging both time series with a moving window of variable width (Fig. S12a). This exercise demonstrates that the transfer function between the Ekman transport away from the Antarctic subpolar seas and the regional SSH anomaly is essentially constant at $\sim 3.8 \times 10^{-4}$ mm (Gt yr^{-1})$^{-1}$ for periods of one year to longer than a decade. The values of the transfer function are calculated simply as the linear fit between Ekman transport and Antarctic coastal sea level for each temporal resolution.

This method of assessment of the relationship between Antarctic coastal sea level and the cross-boundary Ekman transport suffers from both a lack of resolution of sub-annual time scales and the temporal aliasing issues outlined above. To assess the robustness of our basic result, we repeat the analysis with the mean SSH anomaly in the ~5% of the Antarctic subpolar seas that is permanently ice-free (Fig. S12b), permitting a consideration of sub-annual timescales. The resulting transfer function shows relatively modest variability, ranging from 1×10^{-4} to 3×10^{-4} mm (Gt yr^{-1})$^{-1}$ for periods of 2 months to longer than a decade, where the different value of the transfer function simply reflects its relevance to a different area. Thus, we conclude that our estimate of the transfer function in Figure S12a is likely to be robust and representative of the sensitivity of the mean SSH anomaly in the Antarctic subpolar seas to changes in wind forcing.

Bibliography

30 Ablain, M., Cazenave, A., Valladeau, G. & Guinehut, S. A new assessment of the error budget of global mean sea level rate estimated by satellite altimetry over 1993-2008. *Ocean Sci.* **5**, 193-201,

31 Beckley, B.D., Lemoine, F.G., Luthcke, S.B., Ray, R.D., Zelensky N.P., A reassessment of global and regional mean sea level trends from TOPEX and Jason-1 altimetry based on revised reference frame and orbits. *Geophys. Res. Lett.* **34**, L14608

32 Prandi, P., Ablain, M., Cazenave, A. & Picot, N. Sea level variability in the Arctic Ocean observed by satellite altimetry. *Ocean Sci.* **9**, 2375-2401,

33 Beckley, B. D. Zelensky, N. P. Holmes, S. A., Lemoine, F. G. Ray, R. D. Mitchum, G. T. Desai S. D. & Brown S. T. Assessment of the Jason-2 Extension to the TOPEX/Poseidon, Jason-1 Sea-Surface Height Time Series for Global Mean Sea Level Monitoring. *Marine Geodesy* **33,**

34 Prandi, P., Ablain, M., Cazenave, A. & Picot, N. A. New Estimation of Mean Sea Level in the Arctic Ocean from Satellite Altimetry. *Mar. Geodesy* **35**, 61-81,

35 Stammer, D. Response of the global ocean to Greenland and Antarctic ice melting. *J. Geophys. Res.* **113**, C06022

36 Lorbacher, K., Marsland, S. J., Church, J. A., Griffies, S. M. & Stammer, D. Rapid barotropic sea level rise from ice sheet melting. *J. Geophys. Res.* **117**, C06003

37 Tamisiea, M. E.. 2011 Ongoing glacial isostatic contributions to observations of sea level change. *Geophysical Journal International*, **186** (3), 1036-1044,

38 Chambers, D.P., Wahr, J., Tamisiea, M.E., and Nerem R.S. Ocean mass from GRACE and glacial isotactic adjustment. *J. Geophys. Res.: Solid Earth* **115**, B11, B11415

39 Wunsch, C., Ponte, R. M. & Heimbach, P. Decadal trends in sea level patterns: 1993-2004. *J. Clim.* **20**, 5889-5911,

40 Madec, G. NEMO ocean engine. *Note du Pole de modélisation, Institut Pierre-Simon Laplace (IPSL)* **27** (2008).

41 Danabasoglu, G., et al., North Atlantic Simulations in Coordinated Ocean-ice

Reference Experiments phase II (CORE-II). Part I: Mean States, Ocean Modelling, 73 (2014) 76-107,

42 Ridgway K.R., Dunn, J.R. and Wilkin, J.L. Ocean interpolation by four-dimensional least squares; Application to the waters around Australia. *Journal of Atmospheric and Oceanic Technology* ***19***, 9, 1357-1375, (2002)

43 Barrier, N., Treguier A., Cassou C., Deshayes J. Impact of the winter North-Atlantic weather regimes on subtropical sea-surface height variability *Climate Dynamics* **41**, 1159-1171.

44 Reynolds, R. W., Smith, T. M. Liu, C. Chelton, D. B. Casey, K. S. & Schlax, M. G. Daily high-resolution blended analyses for sea surface temperature. *J. Clim*. **20**, 5473-5496,).

45 Jacobs, Stanley S., Claudia F. Giulivi, Large Multidecadal Salinity Trends near the Pacific–Antarctic Continental Margin. *J. Clim.* **23**, 4508–4524,

46 Masson-Delmotte, V. *et al.* Past and future polar amplification of climate change: climate model intercomparisons and ice-core constraints. *Clim. Dyn.* **26**, 513-529,

47 Genthon, C., Krinner, G. & Castebrunet, H. Antarctic precipitation and climate-change predictions: horizontal resolution and margin vs plateau issues. *Ann. Glaciol.* **50**, 55-60,

48 Massonnet, F. *et al.* A model reconstruction of the Antarctic sea ice thickness and volume changes over 1980-2008 using data assimilation. *Ocean Model.* **64**, 67-75,

49 Rintoul, S. R., Hughes, C. W. & Olbers, D. The Antarctic Circumpolar Current system. In *Ocean Circulation and Climate*, Academic Press, San Diego, pp. 271–302 (2001).

50 Dee, D. *et al.* The ERA-Interim reanalysis: Configuration and performance of the data assimilation system. *Quart. J. Roy. Met. Soc.* **137**, 553-597,

51 Bromwich, D. H., Nicolas, J. P. & Monaghan, A. J. An assessment of precipitation changes over Antarctica and the Southern Ocean since 1989 in contemporary global reanalyses. *J. Clim.* **24**, 4189-4209,

52 Holland, P. R. & Kwok, R. Wind-driven trends in Antarctic sea ice drift. *Nature Geosci*. **5**, 872-875,

53 Bracegirdle, T. J. & Marshall, G. J. The reliability of Antarctic tropospheric pressure and temperature in the latest global reanalyses. *J. Clim.* **25**, 7138-7146,

Figure Legends

Figure S1 | Significance of Antarctic subpolar sea linear trend in SSH anomaly. Green shading indicates the area in which the anomalous linear trend in SSH (Fig. 1) is significantly different from zero with 95% confidence, determined using the Patterson t-test accounting for auto-covariance under the assumption of negligible systematic error.

Figure S2 | Linear trend in SSH anomaly in the western Ross Sea for individual satellite missions. The global-mean rate of sea level rise is not removed for simplicity, and the bin-averaging box is indicated in the inset. ERS-1 (black), ERS-2 (dark blue) and Envisat (green) records are shown alongside the Antarctic subpolar sea mean SSH anomaly, including the rate of global-mean sea level rise (light blue). The average linear trend in the western Ross Sea box for the gridded AVISO data set is ~6 mm yr^{-1}. The uncertainties for the single-mission trends are estimated using a bootstrap method accounting for the standard deviation of SSH within the box for each time step.

Figure S3 | GIA corrections for the AVISO-MSLA altimetry data. Left: the correction made to altimetry data associated with the Tamisiea (2011) GIA model. Right: the (highly uncertain) correction for recent ice mass loss, predominantly from the Antarctic Peninsula, computed from Tamisiea (2011) GIA correction and Chambers (2010) GRACE-derived geoid data.

Figure S4 | Time series of Antarctic subpolar sea SSH anomaly showing continuously sea ice-free record. The circumpolar mean of the SSH anomaly south of the oceanic boundary of the Antarctic coastal sea level rise signal (Fig. 1) is indicated in red. Data gaps show times of widespread sea ice cover. The mean of the SSH anomaly in a small subset of the Antarctic subpolar seas that is permanently sea ice-free is indicated in black. Both data sets have had the global-mean rate of sea level rise subtracted.

Figure S5 | Regional anomaly in summer (January to April) linear sea level trend, 1992-2011, relative to the global barystatic rate of sea level rise. As in Figure 1a, the black line demarks the northern boundary of the Antarctic coastal sea level rise anomaly. Markers indicate the location of *in situ* estimates of interdecadal freshening, shaded by the magnitude of the corresponding halosteric sea level rise. The reference for and information synthesised by each marker are given in the table in Figure 1c. The 3000-m isobath is shown in green.

Figure S6 | A decomposition of the NEMO-simulated linear trend in Antarctic subpolar sea steric height anomaly. a. Upper-ocean (0-800 m) trend in halosteric height. b. Deep (> 800 m) trend in halosteric height. c. Upper-ocean (0-800 m) trend in thermosteric height. d. Deep (> 800 m) trend in thermosteric height. The green contours show the 3000-m isobath.

Figure S7 | Comparison of bottom temperature and salinity in the NEMO model and the CARS Southern Ocean climatology. a. and c. show bottom salinity and temperature distributions from the CARS Southern Ocean climatology. b. and d. indicate bottom salinity and temperature distributions estimated from the NEMO model.

Figure S8 | Comparison between zonal-mean sections of salinity in the CARS climatology and the NEMO model. The zonal-mean salinity distributions for CARS (upper) and NEMO (lower), with σ-4 density contours.

Figure S9 | Comparison between zonal-mean sections of temperature in the CARS climatology and the NEMO model. The zonal-mean temperature distributions for CARS (upper) and NEMO (lower), with σ-4 density contours.

Figure S10 | Time series of Ekman transport into the Antarctic subpolar seas. Full lines show the monthly and yearly-averaged Ekman transport into the Antarctic subpolar seas, with the dashed line indicating the linear fit to the yearly averaged data.

Figure S11 | Relationship between the Ekman transport into the Antarctic subpolar seas and regional SSH anomaly. The circles indicate monthly averaged values of the two variables (AASS: Antarctic subpolar seas). The solid line shows the linear fit to the circles, with the 2σ uncertainty denoted by the dashed lines. The rectangle has sides of length defined by uncertainties in the trends in both variables, and indicates the area of Ekman transport - sea level space that the solid line would have to pass through in order for the observed trend in regional SSH anomaly to be explained by wind forcing.

Figure S12 | Time scale dependence of the transfer function between changes in the Ekman transport across the northern boundary of the Antarctic subpolar seas (Fig. 1) and the regional SSH anomaly. The upper panel illustrates results using SSH anomaly measurements in the entire Antarctic subpolar seas, and the lower panel shows results derived from the SSH anomaly record in the subset of the Antarctic subpolar seas that is permanently sea ice-free. The transfer function was estimated by averaging the time series of Ekman transport and SSH anomaly in temporal bins of variable length (indicated by the horizontal axis in both panels) and calculating the linear gradient of the resulting Ekman transport versus Antarctic subpolar seas SSH anomaly distribution.

Figure S13 | Barystatic relative sea level rise resulting from glacial melt between 2003 and 2009. Derived from GRACE gravitometry (Riva et al., 2010).

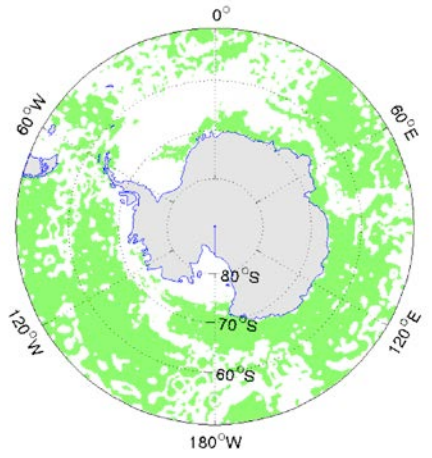

Figure S1 | Significance of Antarctic subpolar sea linear trend in SSH anomaly. Green shading indicates the area in which the anomalous linear trend in SSH (Fig. 1) is significantly different from zero with 95% confidence, determined using the Patterson t-test accounting for auto-covariance under the assumption of negligible systematic error.

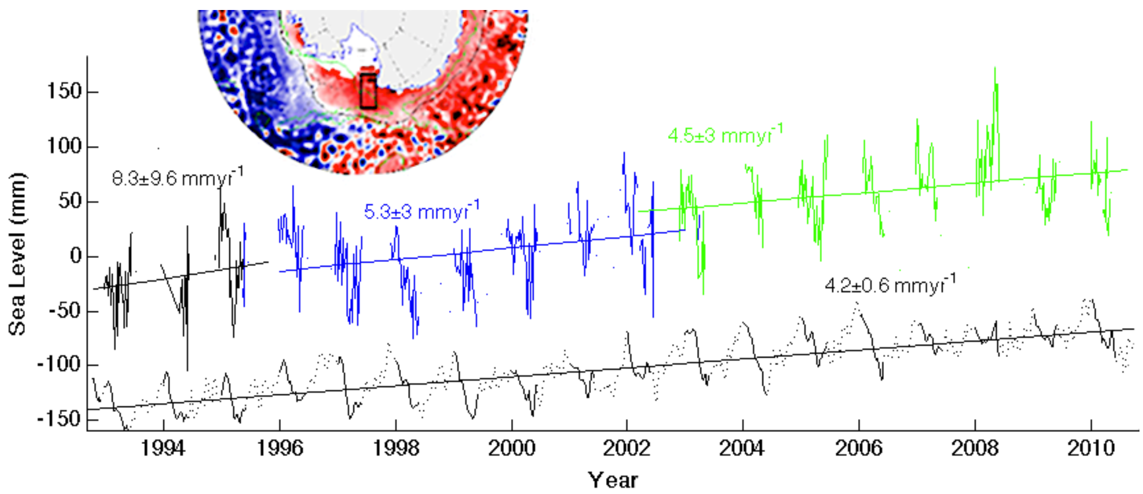

Figure S2 | Linear trend in SSH anomaly in the western Ross Sea for individual satellite missions. The global-mean rate of sea level rise is not removed for simplicity, and the bin-averaging box is indicated in the inset. ERS-1 (black), ERS-2 (dark blue) and Envisat (green) records are shown alongside the Antarctic subpolar sea mean SSH anomaly, including the rate of global-mean sea level rise (light blue). The average linear trend in the western Ross Sea box for the gridded AVISO data set is ~6 mm yr^{-1}. The uncertainties for the single-mission trends are estimated using a bootstrap method accounting for the standard deviation of SSH within the box for each time step.

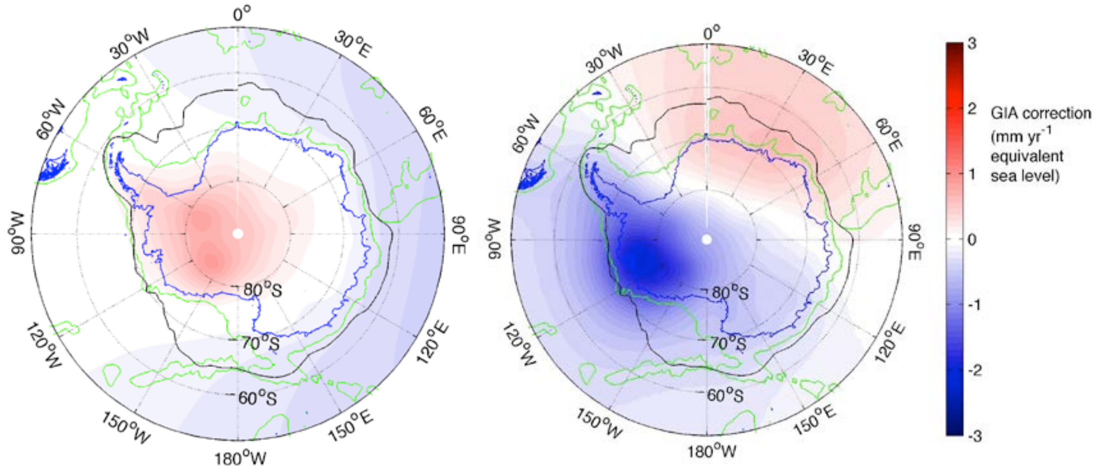

Figure S3 | GIA corrections for the AVISO-MSLA altimetry data. Left: the correction made to altimetry data associated with the Tamisiea (2011) GIA model. Right: the (highly uncertain) correction for recent ice mass loss, predominantly from the Antarctic Peninsula, computed from Tamisiea (2011) GIA correction and Chambers (2010) GRACE-derived geoid data.

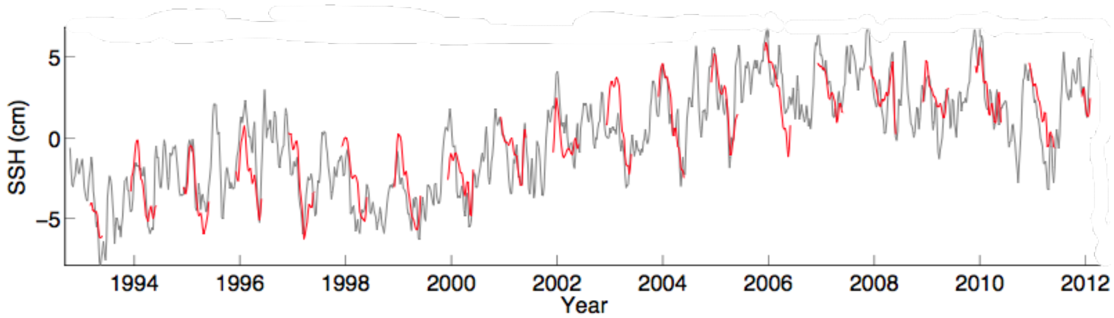

Figure S4 | Time series of Antarctic subpolar sea SSH anomaly showing continuously sea ice-free record. The circumpolar mean of the SSH anomaly south of the oceanic boundary of the Antarctic coastal sea level rise signal (Fig. 1) is indicated in red. Data gaps show times of widespread sea ice cover. The mean of the SSH anomaly in a small subset of the Antarctic subpolar seas that is permanently sea ice-free is indicated in black. Both data sets have had the global-mean rate of sea level rise subtracted.

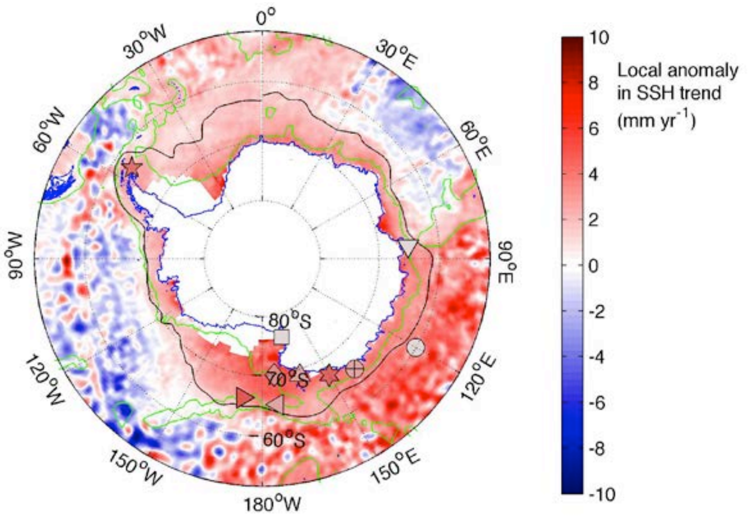

Figure S5 | Regional anomaly in summer (January to April) linear sea level trend, 1992-2011, relative to the global barystatic rate of sea level rise. As in Figure 1a, the black line demarks the northern boundary of the Antarctic coastal sea level rise anomaly. Markers indicate the location of *in situ* estimates of interdecadal freshening, shaded by the magnitude of the corresponding halosteric sea level rise. The reference for and information synthesised by each marker are given in the table in Figure 1c. The 3000-m isobath is shown in green.

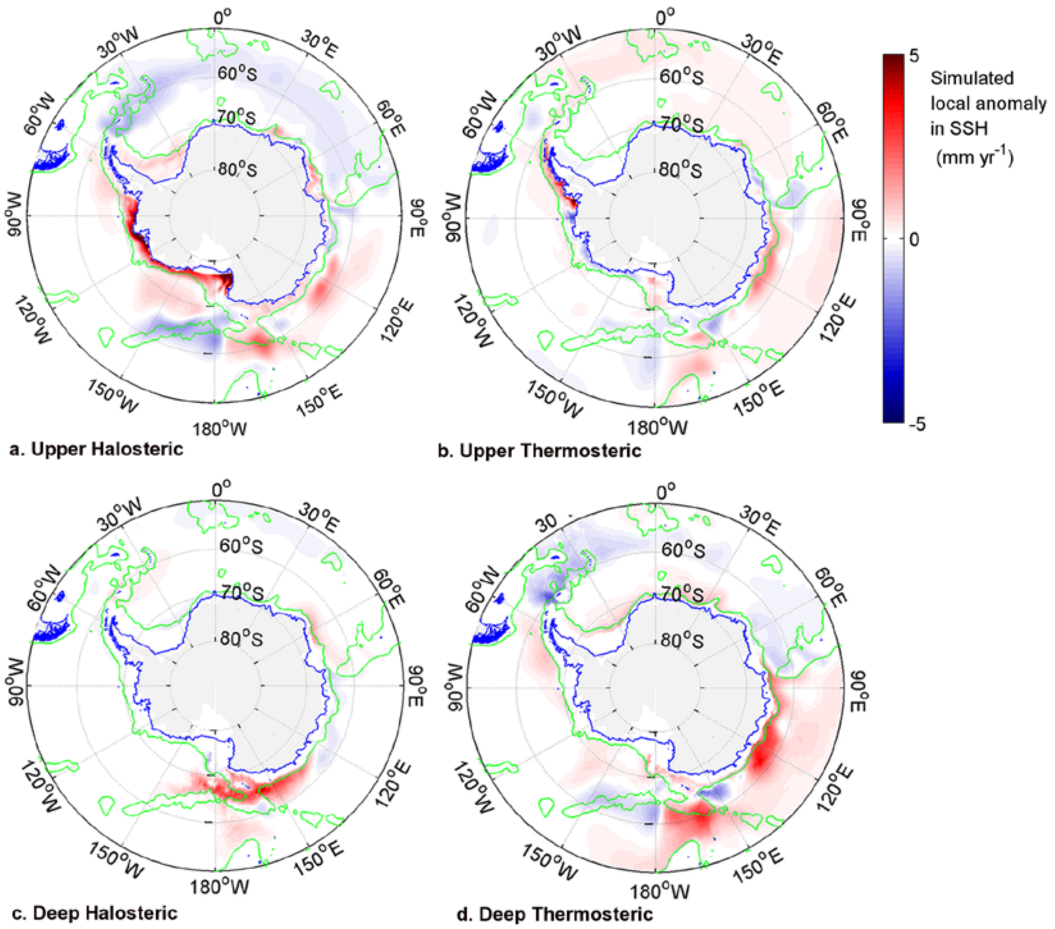

Figure S6 | A decomposition of the NEMO-simulated linear trend in Antarctic subpolar sea steric height anomaly. a. Upper-ocean (0-800 m) trend in halosteric height. b. Deep (> 800 m) trend in halosteric height. c. Upper-ocean (0-800 m) trend in thermosteric height. d. Deep (> 800 m) trend in thermosteric height. The green contours show the 3000-m isobath.

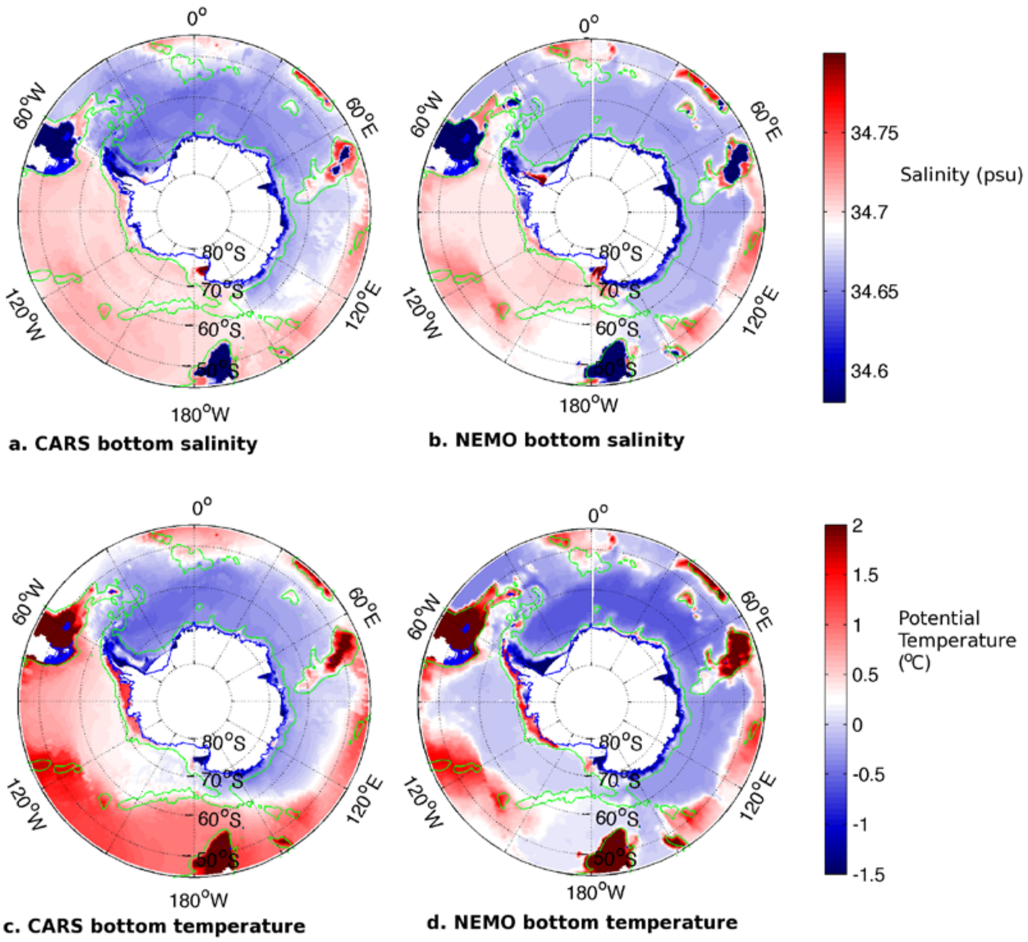

Figure S7 | Comparison of bottom temperature and salinity in the NEMO model and the CARS Southern Ocean climatology. a. and c. show bottom salinity and temperature distributions from the CARS Southern Ocean climatology. b. and d. indicate bottom salinity and temperature distributions estimated from the NEMO model.

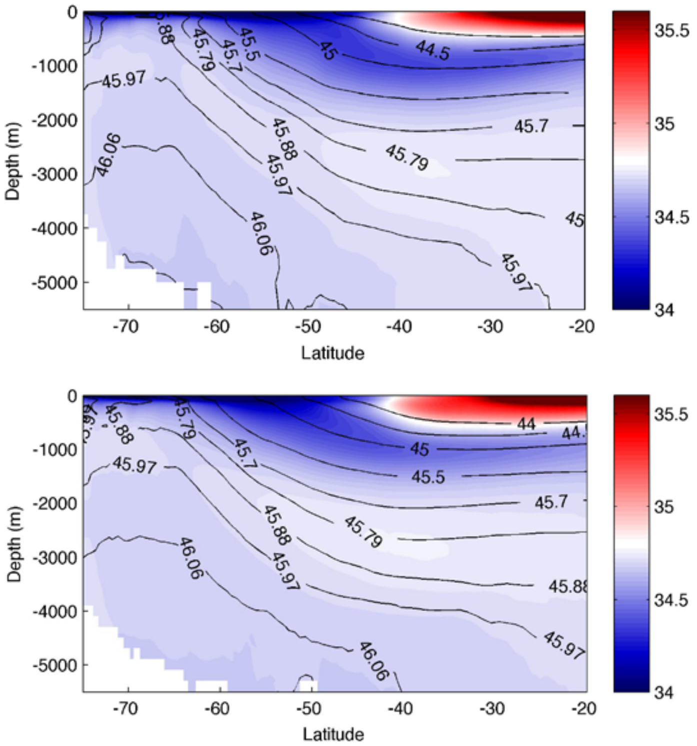

Figure S8 | Comparison between zonal-mean sections of salinity in the CARS climatology and the NEMO model. The zonal-mean salinity distributions for CARS (upper) and NEMO (lower), with σ-4 density contours.

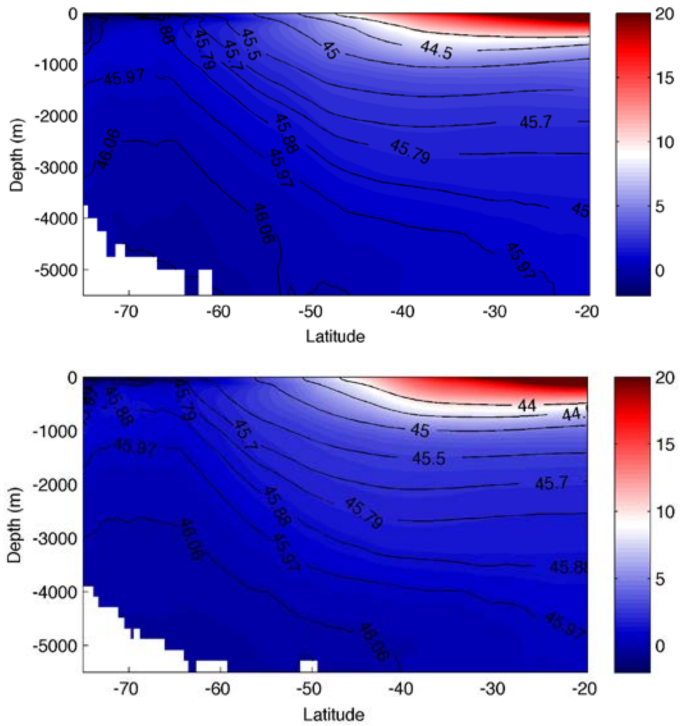

Figure S9 | Comparison between zonal-mean sections of temperature in the CARS climatology and the NEMO model. The zonal-mean temperature distributions for

CARS (upper) and NEMO (lower), with σ-4 density contours.

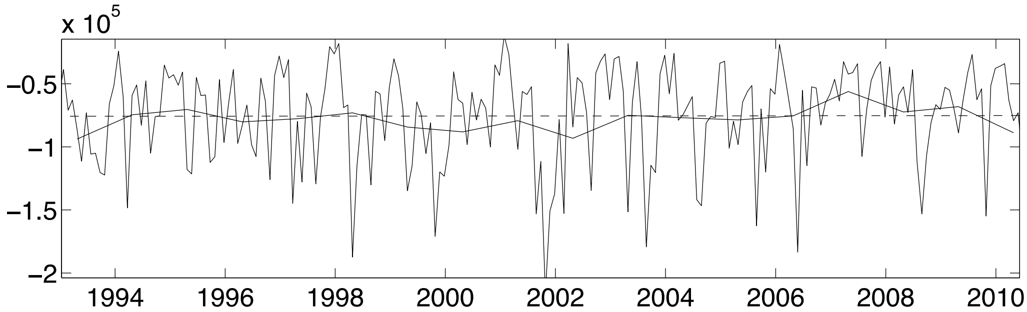

Figure S10 | Time series of Ekman transport into the Antarctic subpolar seas. Full lines show the monthly and yearly averaged Ekman transport into the Antarctic subpolar seas, with the dashed line indicating the linear fit to the yearly averaged data.

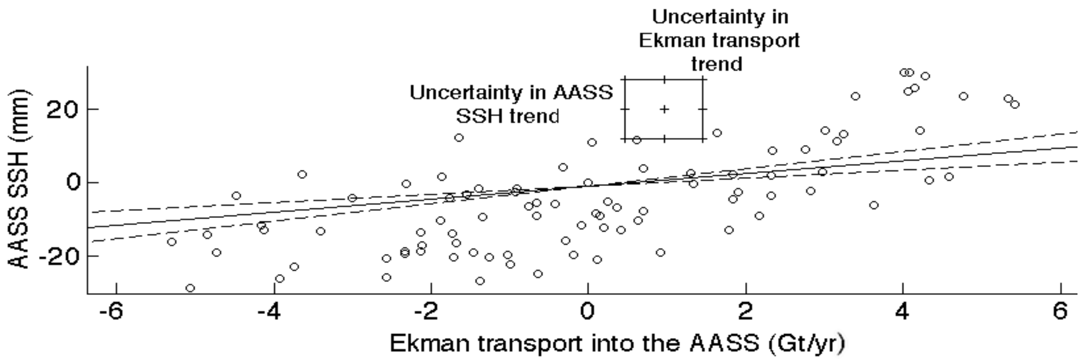

Figure S11 | Relationship between the Ekman transport into the Antarctic subpolar seas and regional SSH anomaly. The circles indicate monthly averaged values of the two variables (AASS: Antarctic subpolar seas). The solid line shows the linear fit to the circles, with the 2σ uncertainty denoted by the dashed lines. The rectangle has sides of length defined by uncertainties in the trends in both variables, and indicates the area of Ekman transport - sea level space that the solid line would have to pass through in order for the observed trend in regional SSH anomaly to be explained by wind forcing.

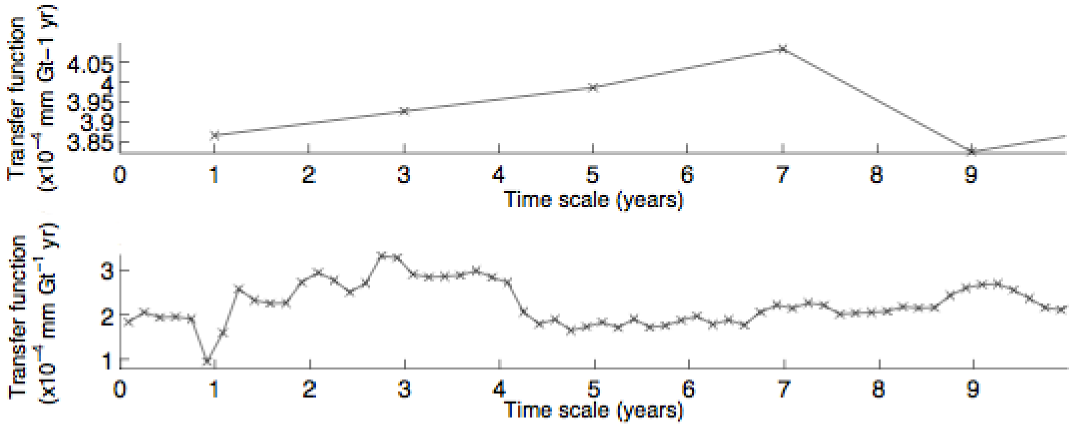

Figure S12 | Time scale dependence of the transfer function between changes in the Ekman transport across the northern boundary of the Antarctic subpolar seas (Fig. 1) and the regional SSH anomaly. The upper panel illustrates results using SSH anomaly measurements in the entire Antarctic subpolar seas, and the lower panel shows results derived from the SSH anomaly record in the subset of the Antarctic subpolar seas that is permanently sea ice-free. The transfer function was estimated by averaging the time series of Ekman transport and SSH anomaly in temporal bins of variable length (indicated by the horizontal axis in both panels) and calculating the linear gradient of the resulting Ekman transport versus Antarctic subpolar seas SSH anomaly distribution.

Figure S13 | Barystatic relative sea level rise resulting from glacial melt between 2003 and 2009. Derived from GRACE gravitometry (Riva et al., 2010).